INTERNATIONAL JOURNAL FOR NUMERICAL METHODS IN FLUIDS
Int. J. Numer. Meth. Fluids 2004; **45**:643–657 (DOI: 10.1002/fld.721)

Boundary-fitted non-linear dispersive wave model for regions of arbitrary geometry

S. Beji*,† and B. Barlas

Department of Naval Architecture and Ocean Engineering, Istanbul Technical University, Maslak 34469, Istanbul, Turkey

SUMMARY

A vertically integrated non-linear dispersive wave model is expressed in non-orthogonal curvilinear co-ordinate system for simulating shallow or deep water wave motions in regions of arbitrary geometry. Both dependent and independent variables are transformed so that an irregular physical domain is converted into a rectangular computational domain with contravariant velocities. Thus, the wall condition for enclosures surrounding a typical physical domain, such as a channel, port or harbor, is satisfied accurately and easily. The numerical scheme is based on staggered grid finite-difference approximations, which result in implicit formulations for the momentum equations and semi-explicit formulation for the continuity equation. Test cases of linear wave propagation in converging, diverging and circular channels are performed to check the reliability of model simulations against the analytical solutions. Cnoidal waves of different steepness values in a circular channel are also considered as examples to non-linear wave propagation within curved walls. In closing, remarks concerning versatility and practical uses of the numerical model are made. Copyright © 2004 John Wiley & Sons, Ltd.

KEY WORDS: water waves; non-linearity; dispersion; boundary-fitted co-ordinates

1. INTRODUCTION

Adoption of curvilinear co-ordinates in engineering problems involving irregular lateral boundaries began in the early 1980s and since then continued in an expanding manner. Through the years, appropriate arrangement of the transformed governing equations and their numerical treatment have been worked out in different contexts for revealing the most suitable techniques and obtaining the most reliable results. Today, the overall approach to numerical solution of an engineering problem in boundary fitted curvilinear co-ordinates is more or less a well-established procedure [1, 2].

*Correspondence to: S. Beji, Department of Naval Architecture and Ocean Engineering, Istanbul Technical University, Maslak 34469, Istanbul, Turkey.
†E-mail: sbeji@itu.edu.tr

Contract/grant sponsor: ITU Research Funding Programme

Published online 4 May 2004

Received 21 August 2003
Revised 22 January 2004

Earlier attempts of formulating circulation or tidal wave models in boundary-fitted co-ordinates focused on the geometrical transformation alone (i.e. the transformation of the independent variables only) thus keeping the original Cartesian velocities as dependent variables [3–5]. Later studies revealed that use of the Cartesian velocities introduces definite numerical restrictions and inaccuracies (see Reference [6] for more details). For a circulation model Sheng [7] was the first to transform both the dependent and the independent variables hence expressing the equations in terms of contravariant velocities.

A three-dimensional tidal wave model in boundary-fitted co-ordinates with a σ-stretching in the vertical co-ordinate was presented by Bao *et al.* [8]. Hsu *et al.* [9] formulated a depth-averaged curvilinear free surface model in two dimensions for open channel flows. Li and Zhan's [10] work on an improved Boussinesq model in boundary-fitted co-ordinates may be considered as a notable exception to non-dispersive wave models. Romanenkov *et al.* [11] investigated the effects of using different velocity variables in viscous shallow-water equations, and, quite recently, Sankaranarayanan and Spaulding [12] studied the effects of grid non-orthogonality on the solution of shallow water equations in boundary-fitted co-ordinate systems.

The present work contributes to a relatively less exploited application area of the curvilinear co-ordinate transformations and expresses a non-linear-dispersive wave model, valid for arbitrary relative depths, in curvilinear co-ordinates in terms of the contravariant velocities. The transformation is accomplished in the simplest manner possible by re-arranging the original wave equations in forms suitable for straightforward transformations. A second-order radiation condition, which includes Sommerfeld's radiation condition as special case, is also expressed in curvilinear co-ordinates for use as outgoing boundary condition. The resulting transformed equations are then numerically solved using finite-difference approximations with staggered girds. Use of contravariant velocities is found to be particularly advantageous for physical domains involving walls with curved surfaces. Several tests are considered for checking the reliability of the numerical scheme. First, linear long wave propagation across a channel of gradually varying cross-section is simulated to compare the amplitude variations against Green's analytical formula. Wave simulations in a circular channel is considered next to compare the numerically obtained solutions with the exact analytical solutions. The results for all these test cases show almost perfect agreement between the analytical and the numerical solutions. Finally, cnoidal waves of different wave steepness values in a circular channel are considered as examples to non-linear wave transformations in irregular geometries. Prominent features of the non-linear simulations are emphasized. In closing, comments are made on possible practical applications and extensions of the present model to more realistic wave conditions, such as breaking.

2. TRANSFORMATION OF WAVE MODEL

The wave model used in this work is the one-component form of the fully dispersive non-linear model of Nadaoka *et al.* [13]. The model is operational for both shallow and deep water waves; hence, it can reproduce the cnoidal and the second-order Stokes waves equally well, besides simulating narrow-banded non-linear random waves over arbitrary depths. The continuity equation, and x- and y-component of the momentum equation, when expressed in

suitable forms for the transformations, may be written as

$$\zeta_t + [(C_p^2/g + \zeta)u]_x + [(C_p^2/g + \zeta)v]_y = 0 \tag{1}$$

$$ru_t + \left[g\zeta + \frac{1}{2}(1 - 3\omega^2 C_p^2/g^2)(u^2 + v^2)\right]_x = \frac{1}{\omega^2 C_p^2}[C_p^4(1 - r)(u_x + v_y)_t]_x \tag{2}$$

$$rv_t + \left[g\zeta + \frac{1}{2}(1 - 3\omega^2 C_p^2/g^2)(u^2 + v^2)\right]_y = \frac{1}{\omega^2 C_p^2}[C_p^4(1 - r)(u_x + v_y)_t]_y \tag{3}$$

where ζ is the free surface elevation, u and v are the Cartesian components of the horizontal velocity vector at the still water level $z = 0$, and g is the gravitational acceleration. C_p and C_g are, respectively, the phase and group velocities computed according to linear theory for a specified wave frequency ω and a given local depth h, and $r = C_g/C_p$. A subscript stands for partial differentiation with respect to the indicated variable. The non-linear terms ζw_t and w^2 in Equations (2) and (3) have been re-expressed as $\zeta w_t = -(\omega^2 C_p^2/g^2)(u^2 + v^2)$ and $w^2 = -(\omega^2 C_p^2/g^2)(u^2 + v^2)$ using the zeroth-order relations $\zeta = \pm(C_p/g)(u^2 + v^2)^{1/2}$ and $w = \zeta_t = \mp i\omega\zeta = \mp i(\omega C_p/g)(u^2 + v^2)^{1/2}$ (see Reference [14]) for facilitating the rearrangement of the equations in the above forms.

Coordinate transformations from a two-dimensional Cartesian system (x, y, t) to a two-dimensional curvilinear system (ξ, η, τ) are given by [1]

$$\frac{\partial}{\partial x} = \xi_x \frac{\partial}{\partial \xi} + \eta_x \frac{\partial}{\partial \eta}, \qquad \frac{\partial}{\partial y} = \xi_y \frac{\partial}{\partial \xi} + \eta_y \frac{\partial}{\partial \eta}, \qquad \frac{\partial}{\partial t} = \frac{\partial}{\partial \tau} \tag{4}$$

in which the metrics are defined as

$$\xi_x = Jy_\eta, \qquad \xi_y = -Jx_\eta, \qquad \eta_x = -Jy_\xi, \qquad \eta_y = Jx_\xi \tag{5}$$

with $J = (x_\xi y_\eta - x_\eta y_\xi)^{-1}$ being the Jacobian of the transformation.

From Equations (1)–(3) it is obvious that expressing $u_x + v_y$ and $u^2 + v^2$ in curvilinear co-ordinates in terms of the contravariant velocities would basically complete the transformation process. Making use of (4) and (5), denoting the contravariant velocity components in the ξ- and η-directions by U and V while noting that they are defined as $U = J(y_\eta u - x_\eta v)$ and $V = J(-y_\xi u + x_\xi v)$, gives

$$u_x + v_y = J(U_\xi^* + V_\eta^*) \tag{6}$$

$$u^2 + v^2 = (\eta_x^2 + \eta_y^2)U^{*2} + (\xi_x^2 + \xi_y^2)V^{*2} - 2(\xi_x\eta_x + \xi_y\eta_y)U^*V^* \tag{7}$$

where U^* and V^* are defined as $U^* = U/J$, $V^* = V/J$ for notational convenience.

The continuity equation is transformed in a manner quite similar to Equation (6) and therefore no detail is given here. The momentum equations in the ξ- and η-direction are obtained by combining the x- and y-momentum equation as follows. Substitute (6) and (7) into (2) and (3), then multiply (2) by ξ_x, (3) by ξ_y, and finally add the resulting equations to get the ξ-momentum equation. In a similar vein, multiply (2) by η_x, (3) by η_y, and add the equations to get the η-momentum equation. Thus, the wave model in curvilinear co-ordinates in terms of the contravariant velocity components $U^* = U/J$ and $V^* = V/J$ becomes

$$\zeta_\tau + J[(C_p^2/g + \zeta)U^*]_\xi + J[(C_p^2/g + \zeta)V^*]_\eta = 0 \tag{8}$$

$$rJU_\tau^* + \xi_*^2 S_\xi + \xi_*\eta_* S_\eta = \frac{\xi_*^2}{\omega^2 C_p^2}[C_*(U_\xi^* + V_\eta^*)]_{\xi\tau} + \frac{\xi_*\eta_*}{\omega^2 C_p^2}[C_*(U_\xi^* + V_\eta^*)]_{\eta\tau} \tag{9}$$

$$rJV_\tau^* + \xi_*\eta_* S_\xi + \eta_*^2 S_\eta = \frac{\xi_*\eta_*}{\omega^2 C_p^2}[C_*(U_\xi^* + V_\eta^*)]_{\xi\tau} + \frac{\eta_*^2}{\omega^2 C_p^2}[C_*(U_\xi^* + V_\eta^*)]_{\eta\tau} \tag{10}$$

where

$$\begin{aligned} S &= g\zeta + \frac{1}{2}(1 - 3\omega^2 C_p^2/g^2)[\eta_*^2 U^{*2} + \xi_*^2 V^{*2} - 2\xi_*\eta_* U^* V^*] \\ \xi_*^2 &= \xi_x^2 + \xi_y^2, \qquad \eta_*^2 = \eta_x^2 + \eta_y^2 \\ \xi_*\eta_* &= \xi_x\eta_x + \xi_y\eta_y, \qquad C_* = C_p^4(1 - r)J \end{aligned} \tag{11}$$

Note that for the special case of a rectangular physical domain, $\xi_x = 1$, $\xi_y = 0$, $\eta_x = 0$ and $\eta_y = 1$, the above equations become identical with the original equations.

3. BOUNDARY CONDITIONS

Three different boundary conditions are considered: incoming boundary condition, wall condition and outgoing boundary condition. The first two conditions are quite easy to deal with while the outgoing boundary condition requires some care.

At the incoming boundary, which is taken along the η-axis at $\xi = 0$, the free surface displacement ζ is specified by assigning time series of a definite wave form. For unidirectional waves, U^* is obtained from the relation $U^* = (\xi_x u + \xi_y v)/J$, using $u = C\zeta/(C_p^2/g + \zeta)$ and $v = 0$, as dictated by the non-linear continuity equation for unidirectional periodic waves of celerity C, which, for non-linear waves, may be different from C_p used in wave equations. Directional waves at the incoming boundary can still be generated by using these specifications, it is only necessary to introduce an appropriate phase angle for each grid point along the η-axis on the boundary.

Since the wave model is formulated in terms of the contravariant velocities, the wall condition even for irregular geometries can be specified by simply requiring the contravariant velocity component normal to the wall boundary vanish. Thus, unlike models formulated in terms of the Cartesian velocities, no iteration is needed for satisfying the wall condition; consequently the results are more accurate.

The radiation condition for outgoing waves usually requires particular attention due to undesirable reflection effects which contaminate the solution within the domain. For unidirectional waves the classical radiation condition is given by Sommerfeld's equation $u_t \pm Cu_x = 0$, which implies right or left going unidirectional waves of constant celerity C in the x-direction. Various absorbing boundary conditions have been proposed (see for instance, References [15–17]). Among such conditions Engquist and Majda's [15] second-order radiation condition is particularly suitable for the present scheme. For waves moving primarily in the x- and y-directions, respectively, their second-order condition is

$$u_{tt} \pm Cu_{xt} - \frac{1}{2} C^2 u_{yy} = 0, \qquad v_{tt} \pm Cv_{yt} - \frac{1}{2} C^2 v_{xx} = 0 \tag{12}$$

The numerical approach adopted in this work uses only two time levels; hence, time derivatives must not exceed the first order. To meet this requirement the above equations are split as

$$u_t \pm Cu_x = P, \qquad P_t - \frac{1}{2} C^2 u_{yy} = 0 \tag{13}$$

$$v_t \pm Cv_y = Q, \qquad Q_t - \frac{1}{2} C^2 v_{xx} = 0 \tag{14}$$

Note that for $P = Q = 0$, (13) and (14) give Sommerfeld's radiation condition in the x- and y-direction.

Unless some simplifications are introduced the transformations of Equations (13) and (14) to the curvilinear co-ordinates result in quite cumbersome expressions. To this end, assuming an unvarying geometry for the physical domain in the vicinity of the outgoing boundary would be quite plausible, making the derivatives of the metrics zero. With the implementation of this assumption and through appropriate combination of the equations the second-order radiation condition of Engquist and Majda [15] in curvilinear co-ordinates for the ξ-and η-directions becomes

$$\begin{aligned}
&(\xi_x\eta_y - \xi_y\eta_x)U^*_\tau + C[(\xi_x^2\eta_y - \xi_y^2\eta_x)U^*_\xi + \eta_x\eta_y(\xi_x - \xi_y)U^*_\eta] \\
&\quad - C\xi_x\xi_y[(\xi_x - \xi_y)V^*_\xi + (\eta_x - \eta_y)V^*_\eta] = \xi_x P + \xi_y Q
\end{aligned}$$

$$\begin{aligned}
&P_\tau - \frac{1}{2} C^2(\eta_y^3 U^*_{\eta\eta} + 2\xi_y\eta_y^2 U^*_{\xi\eta} + \xi_y^2\eta_y U^*_{\xi\xi}) \\
&\quad + \frac{1}{2} C^2(\xi_y\eta_y^2 V^*_{\eta\eta} + 2\xi_y^2\eta_y V^*_{\xi\eta} + \xi_y^3 V^*_{\xi\xi}) = 0
\end{aligned} \tag{15}$$

$$\begin{aligned}
&(\xi_x\eta_y - \xi_y\eta_x)V^*_\tau + C[(\xi_x\eta_y^2 - \xi_y\eta_x^2)V^*_\eta - \xi_x\xi_y(\eta_x - \eta_y)V^*_\xi] \\
&\quad + C\eta_x\eta_y[(\eta_x - \eta_y)U^*_\eta + (\xi_x - \xi_y)U^*_\xi] = \eta_x P + \eta_y Q
\end{aligned}$$

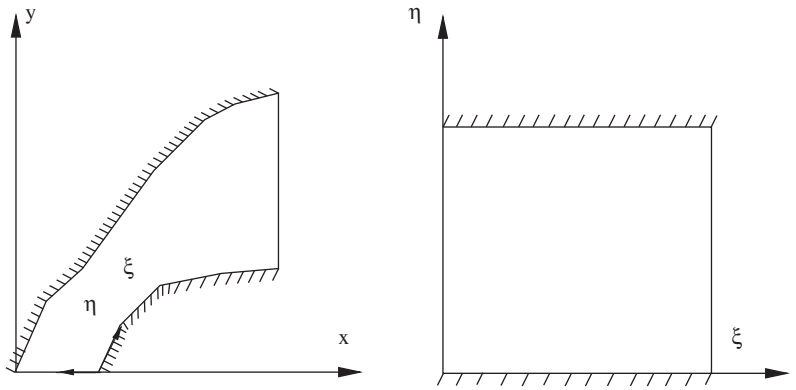

Figure 1. Definition sketch of an arbitrary physical domain (left) and the corresponding computational domain (right). The hatched lines indicate wall boundaries.

$$Q_\tau - \frac{1}{2} C^2(\xi_x^3 V_{\xi\xi}^* + 2\xi_x^2 \eta_x V_{\xi\eta}^* + \xi_x \eta_x^2 V_{\eta\eta}^*) + \frac{1}{2} C^2(\xi_x^2 \eta_x U_{\xi\xi}^* + 2\xi_x \eta_x^2 U_{\xi\eta}^* + \eta_x^3 U_{\eta\eta}^*) = 0 \tag{16}$$

If the physical domain is rectangular, $\xi_x = 1$, $\xi_y = 0$, $\eta_x = 0$ and $\eta_y = 1$; hence, (15) and (16) reduce to (13) and (14), respectively.

While Equations (15) and (16) provide definitely better absorption of directional waves, numerical experiments have revealed that their degenerate forms with $P = 0$ and $Q = 0$ (Sommerfeld's equations) also provide quite acceptable results as long as outgoing waves do not make acute angles with the boundary, as demonstrated for a ring test by Beji and Nadaoka [18].

4. NUMERICAL APPROACH

Regardless of the shape of the physical domain, Equations (8)–(10) are solved in a perfectly rectangular computational domain using finite-difference approximations with unit grid sizes in both directions. Figure 1 shows a sketch of an arbitrary physical domain and the corresponding computational domain. Several different approaches based on the staggered or non-staggered grids are available. After trying three different grid orientations (i.e. non-staggered grid, staggered Arakawa B-grid, and staggered Arakawa C-grid [19]) it has been decided that staggered Arakawa C-grid performed best for the equations used here. Figure 2 shows the grid orientation for the variables. All the derivatives are centred at the mid-time level $t + \Delta t/2$, t being the current time and Δt the time step. The main wave propagation direction is taken along the positive ξ-axis; therefore, ξ-momentum equation is solved first to obtain U^* for the new time level $t + \Delta t$, assuming the new time level values of ζ and V^* known. In accordance

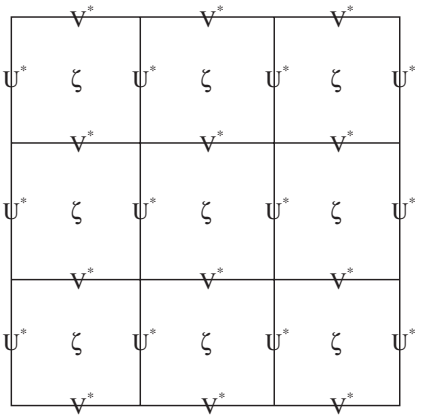

Figure 2. Grid orientation (staggered Arakawa C-grid) for the variables ζ, U^* and V^*.

with the grid system shown in Figure 2 the ξ-direction derivatives are discretized as

$$U_\xi^* = \frac{U_{i+1,j}^{*k+1} - U_{i-1,j}^{*k+1} + U_{i+1,j}^{*k} - U_{i-1,j}^{*k}}{4}, \qquad S_\xi = \frac{S_{i+1,j}^{k+1} - S_{i,j}^{k+1} + S_{i+1,j}^{k} - S_{i,j}^{k}}{2}$$
$$V_\xi^* = \frac{V_{i+1,j}^{*k+1} - V_{i,j}^{*k+1} + V_{i+1,j-1}^{*k+1} - V_{i,j-1}^{*k+1} + V_{i+1,j}^{*k} - V_{i,j}^{*k} + V_{i+1,j-1}^{*k} - V_{i,j-1}^{*k}}{4} \tag{17}$$

where i and j denote the indices in the ξ- and η- directions while k indicates the time level. η-momentum equation is then solved for V^* using the new U^* values as computed from the previous step. Likewise, the η- direction derivatives are discretized as

$$V_\eta^* = \frac{V_{i,j+1}^{*k+1} - V_{i,j-1}^{*k+1} + V_{i,j+1}^{*k} - V_{i,j-1}^{*k}}{4}, \qquad S_\eta = \frac{S_{i,j+1}^{k+1} - S_{i,j}^{k+1} + S_{i,j+1}^{k} - S_{i,j}^{k}}{2}$$
$$U_\eta^* = \frac{U_{i,j+1}^{*k+1} - U_{i,j}^{*k+1} + U_{i-1,j+1}^{*k+1} - U_{i-1,j}^{*k+1} + U_{i,j+1}^{*k} - U_{i,j}^{*k} + U_{i-1,j+1}^{*k} - U_{i-1,j}^{*k}}{4} \tag{18}$$

Note that in the computational domain $\Delta\xi = \Delta\eta = 1$ as indicated above. The rest of the derivatives are discretized in a similar manner. The velocity computations require solutions of tridiagonal matrix systems, which are accomplished very efficiently by the Thomas algorithm (see Reference [20, p. 40]). The surface displacement is obtained from a semi-explicit discretization (i.e. explicit in ζ, implicit in U^* and V^*) of the continuity equation, which is treated as explicit in the computations. Finally, the radiation condition is implemented through one-sided discretization of the spatial derivatives wherever needed; otherwise they are centred following the usual approach. Since all these computations involve certain approximations, an iterative procedure is needed. Through numerical experiments it has been ascertained that for all the cases considered in this work, a maximum of five iterations were sufficient to obtain reliable results. This was determined by continuously computing the difference between the iteratively computed values of the normalized surface displacement (normalized with respect to the incident wave amplitude) at every discreet point and requiring that the difference be less than 10^{-5}.

5. TEST CASES AND NON-LINEAR WAVE SIMULATIONS

In order to perform checks on the reliability of the model developed, several test cases are considered. Wave simulations in gradually converging, diverging and circular channels are performed for comparisons with the corresponding analytical results while cnoidal waves of different steepness in a circular channel are also simulated as examples to non-linear wave transformations within curved boundaries.

5.1. Linear waves in gradually converging and diverging channels

First, linear long wave propagation across a converging channel is simulated and the magnification of the wave amplitude is compared with the theoretical formula of Green. The period of the incident wave is $T = 10$ s and the water depth is $h = 1$ m, which result in a depth to wavelength ratio of approximately $h/L = \frac{1}{30}$, indicating a long wave. The channel width $b_0 = 30$ m at $x = 0$ m reduces to half its initial value after a distance of 10 wavelengths. For such a varying channel Green's formula (see Reference [21, Section 185]) predicts an amplitude variation according to

$$a(x) = a_0 \sqrt{b_0/b(x)} \tag{19}$$

where a_0 and b_0 are, respectively, the wave amplitude and the channel width at $x = 0$ m while $a(x)$ and $b(x)$ are the corresponding values at an arbitrary location x along the channel. Simulations are performed for $\Delta t = T/40$ s and $\Delta x = L/40$ m thus making the Courant number in the propagation direction $Cr = C\Delta t/\Delta x$ exactly one. The Courant number does not have to be unity; however, numerical trials indicate better results for $Cr = 1$. The crosswise resolution is taken as $\Delta y = b(x)/15$ m while Equation (15) with $P = 0$ (Sommerfeld's equation) is used as the radiation condition at $x = 10L$ m. The grids in the physical domain were not orthogonal since they were generated by making equal and straight divisions in the x- direction and then dividing the corresponding channel widths into equal lengths. Hence, the simulation also works as a check on the non-orthogonal terms. Figure 3(a) shows a perspective view of the fully developed wave field while Figure 3(b) compares the numerically computed wave form along the mid-section with Green's formula.

A counterpart of the above simulation is performed for a diverging channel with identical incident wave and water depth conditions. In contrast to the previous case the channel width doubles its initial value after 10 wavelengths while Green's formula still remains valid as given above. Figure 4(a) shows the perspective view and Figure 4(b) compares the computed and theoretical values as in Figures 3(a) and 3(b). For both cases the agreement with the theory is almost perfect.

5.2. Linear waves in a circular channel

Equations (8)–(10) are now used for the simulation of waves in a circular channel. Since the analytical solution is available only for linear waves the simulations are performed for the linearized versions of the equations first.

In the context of acoustics, Rostafinski [22] studied the sound propagation in a curved duct. The analytical solution, which may be readily adapted to the present problem, is as follows. Surface elevation in polar co-ordinates ($r = \sqrt{x^2 + y^2}$, $\theta = \arctan y/x$) is expressed as a linear

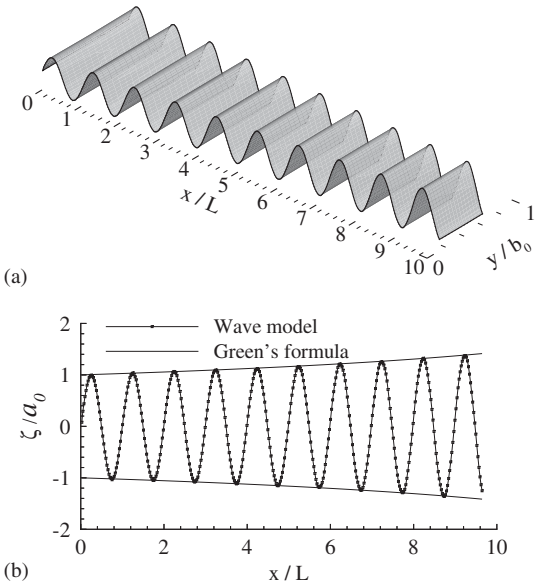

Figure 3. (a) Perspective view of the fully developed wave field in a converging channel; and (b) comparison of the numerically computed amplitude magnification with Green's analytical formula.

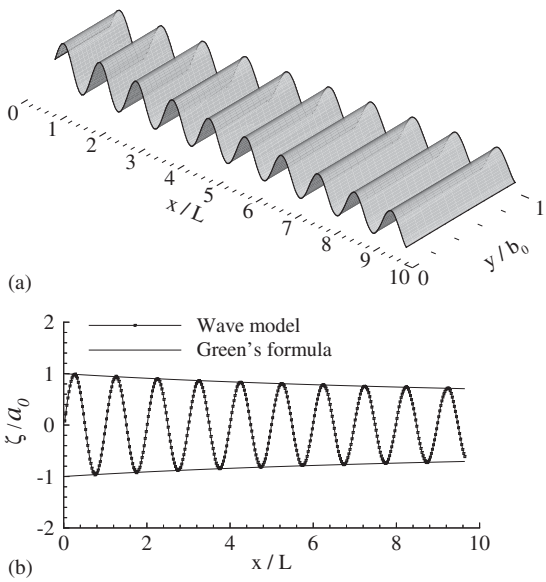

Figure 4. (a) Perspective view of the fully developed wave field in a diverging channel; and (b) comparison of the numerically computed amplitude attenuation with Green's analytical formula.

combination of different modes, which are given in terms of the Bessel functions of the first and second kind:

$$\zeta(r,\theta,t)=\sum_{n=1}^{N}[a_nJ_{\nu_n}(kr)+b_nY_{\nu_n}(kr)]\mathrm{e}^{\mathrm{i}\nu_n\theta}\mathrm{e}^{\mathrm{i}\omega t} \tag{20}$$

where ω is the wave frequency, k is the wave number and the orders ν_n of the Bessel functions are to be determined from Equation (23) below. The boundary conditions on the inner wall $\partial\zeta/\partial r|_{r=r_\mathrm{i}}=0$ and outer wall $\partial\zeta/\partial r|_{r=r_\mathrm{o}}=0$ give, respectively,

$$a_nJ'_{\nu_n}(kr_\mathrm{i})+b_nY'_{\nu_n}(kr_\mathrm{i})=0 \tag{21}$$

$$a_nJ'_{\nu_n}(kr_\mathrm{o})+b_nY'_{\nu_n}(kr_\mathrm{o})=0 \tag{22}$$

in which the primes denote differentiation with respect to r while r_i and r_o denote the inner and outer radii of the circular channel. Eliminating a_n and b_n from the above equations provides the condition for determining ν_n:

$$J'_{\nu_n}(kr_\mathrm{i})Y'_{\nu_\mathrm{n}}(kr_\mathrm{o})-J'_{\nu_n}(kr_\mathrm{o})Y'_{\nu_n}(kr_\mathrm{i})=0 \tag{23}$$

Imposing the incident wave amplitude as $\zeta(r,0,0)=1$ at the channel entrance $\theta=0$, noting that each component function is orthogonal with weight $1/r$, the coefficients a_n and b_n are determined as

$$a_n=Y'_{\nu_n}(kr_\mathrm{i})\frac{\int_{r_\mathrm{i}}^{r_\mathrm{o}}(F_n(r)/r)\mathrm{d}r}{\int_{r_\mathrm{i}}^{r_\mathrm{o}}(F_n^2(r)/r)\mathrm{d}r},\qquad b_n=-\frac{J'_{\nu_n}(kr_\mathrm{i})}{Y'_{\nu_n}(kr_\mathrm{i})}a_n \tag{24}$$

where $F_n(r)=J_{\nu_n}(kr)Y'_{\nu_n}(kr_\mathrm{i})-Y_{\nu_n}(kr)J'_{\nu_n}(kr_\mathrm{i})$ is obtained by solving (21) for b_n and then substituting it into (20). Note that b_n could be expressed using Equation (22) as well.

For the test case considered here the inner radius of the channel is taken as $r_\mathrm{i}=25\,\mathrm{m}$ and the outer radius as $r_\mathrm{o}=50\,\mathrm{m}$: the channel covers an arc of 180°. The water depth and the incident wave period are selected as $h=1\,\mathrm{m}$ and $T=4\,\mathrm{s}$, respectively. These parameters result in a wavelength of $L=12\,\mathrm{m}$ and wave number $k=0.52\,\mathrm{rad/m}$.

Using Equation (20) the analytical solution is established from the superposition of $N=5$ different modes, which are computed as $\nu_n=5.08,12.31,15.14,18.62,23.83$ from Equation (23) for $r_\mathrm{i}=25\,\mathrm{m}$, $r_\mathrm{o}=50\,\mathrm{m}$ and $k=0.52\,\mathrm{rad/m}$.

In the numerical simulations sinusoidal waves with a uniform amplitude are imposed across the channel at the entrance while Equation (15) is used as the radiation condition at the end of the computational domain. In the physical domain, a constant angular grid spacing of $\Delta\theta=\pi/500$ radian is used along the channel while the grid spacing in the radial direction is $\Delta r=1\,\mathrm{m}$. The time resolution is taken as $\Delta t=T/50\,\mathrm{s}$ so that the average Courant number (computed by averaging the arc lengths corresponding to the inner and outer radii) in the wave propagation direction was approximately unity.

As the waves propagate in the circular channel, they reflect from the outer wall and diffract in the vicinity of the inner wall thus creating quite complicated patterns as shown in the perspective views at $t=8T\,\mathrm{s}$ and $t=20T\,\mathrm{s}$ in Figures 5(a) and 5(b), respectively.

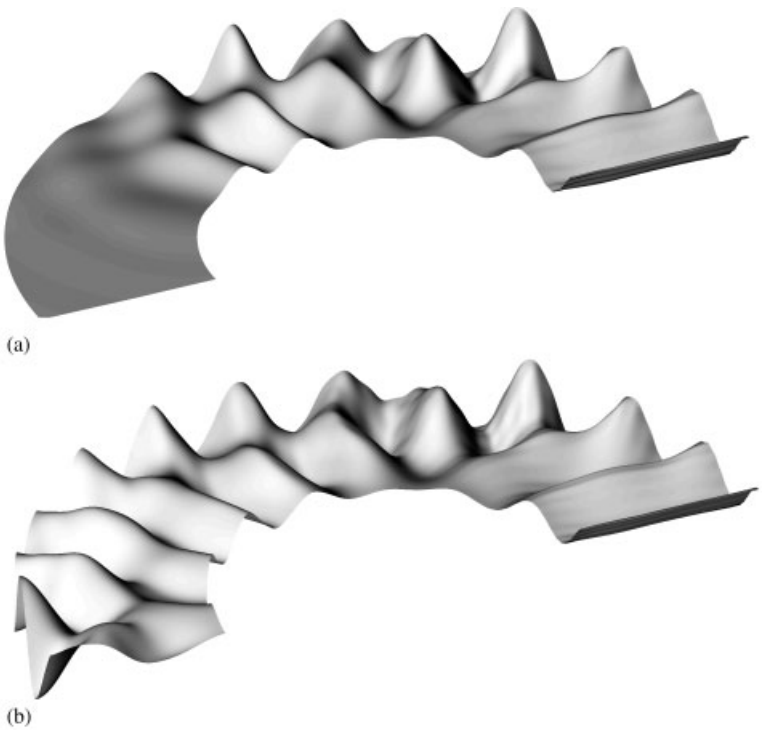

Figure 5. (a) Perspective view of the wave field at $t = 8T$ in a circular channel; and (b) perspective view of the wave field at $t = 20T$ in a circular channel.

In order to make comparisons with the theory, the contours of the analytical solution and the fully developed wave field as obtained from the numerical solution after 20 wave periods elapsed are depicted together in Figure 6. Except for minor differences the two solutions remarkably agree with each other and establish confidence in the model equations and the numerical code.

Finally, comparisons of the surface displacement between the analytical and numerical solution along the inner wall and the outer wall are presented in Figures 7(a) and 7(b). As the figures reveal, the agreement with the theory is excellent even for such a case involving complicated reflection and diffraction patterns. Thus, the test provides a definite conclusion regarding the reliability of the equations derived.

5.3. Cnoidal waves in a circular channel

Korteweg and DeVries [23] coined the word cnoidal for non-linear periodic waves of permanent shape in shallow water. The present wave model is also capable of reproducing the cnoidal waves besides being valid for deep water waves. In order to investigate the effects of non-linearity as well as exploring the capabilities of the present model, simulations of cnoidal waves in a circular channel are carried out. According to the cnoidal wave theory only two

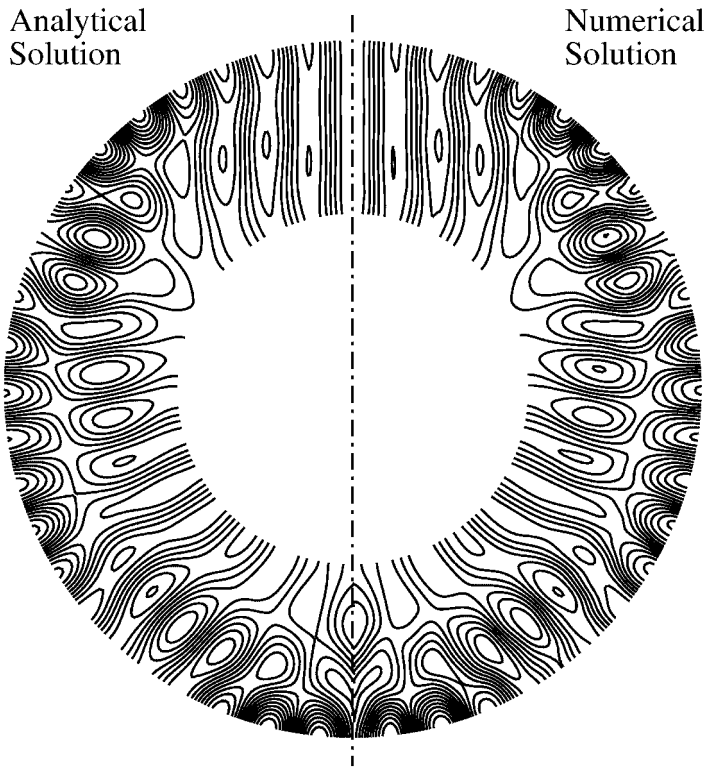

Figure 6. Contours of the analytical solution (left-half) and the numerical solution (right-half) after 20 wave periods.

dimensionless parameters may be selected freely; the rest of the physical quantities, such as wave period, wavelength and celerity are fixed according to these two parameters and the complete elliptic integrals $E(m)$ and $K(m)$ which are defined by $E(m)=\int_0^{\pi/2}(1-m\sin^2\theta)^{1/2}\,\mathrm{d}\theta$ and $K(m)=\int_0^{\pi/2}(1-m\sin^2\theta)^{-1/2}\,\mathrm{d}\theta$ as a function of the modulus m. In principle it is possible to select a definite period and wavelength, and then determine the corresponding wave steepness and modulus, but this approach is quite tedious due to the dependency of $E(m)$ and $K(m)$ on m. Therefore, in the simulations presented here, two different wave steepness values $\varepsilon=H/h$ (H wave height) and modulus m are selected first, and then, taking the water depth $h=1$ m as in the simulation of linear waves, the remaining physical quantities T, L, C and the surface displacement ζ are computed according to the original cnoidal theory [23]. Owing to the reflections from the outer wall, waves become quite steep (as much as five times the initial amplitude); therefore, moderate wave steepness values $\varepsilon=0.1$ and 0.3 are used for the incoming waves. The modulus m for each wave steepness ε is determined by trial and error in such a way as to make the wavelength the same for both cases, which in turn is the same as the linear case $L=12$ m. Accordingly, $m=0.66$ for $\varepsilon=0.1$ and $m=0.95$ for $\varepsilon=0.3$ are used. Numerical conditions (time and space resolutions, etc.) were identical to those used in the linear simulations.

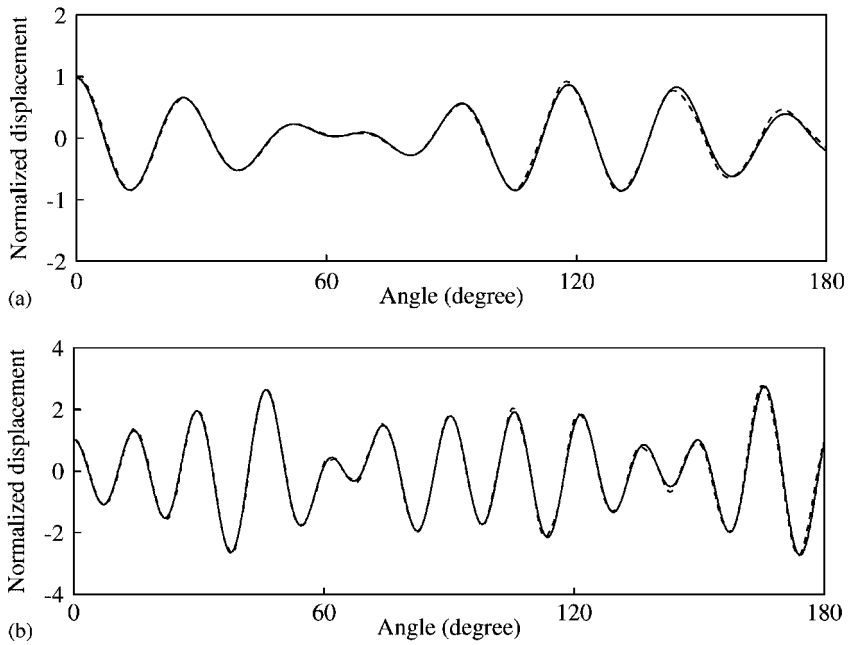

Figure 7. (a) Comparison of the analytical solution (solid line) with the numerical solution (dashed line) at $t = 20T$ along the inner wall of the circular channel; and (b) Comparison of the analytical solution (solid line) with the numerical solution (dashed line) at $t = 20T$ along the outer wall of the circular channel.

Since the dimensions of the circular channel is kept the same for all (linear and cnoidal) simulations it is aimed to maintain a geometric similarity by keeping the wavelength the same as well, for all the cases. In this way, it is possible to observe the prominent features and effects of non-linearity which arise principally from the high wave steepness. Figures 8(a) and 8(b) show the fully developed wave fields for two different wave steepness values. As expected, $\varepsilon = 0.1$ case, being rather weak in non-linearity, resembles the linear case; however, as the wave steepness becomes higher, due to the asymmetric form of the waves, reflections from the outer wall increase considerably and the patters become sharper. For $\varepsilon = 0.3$ the highest point of the normalized surface elevation is very nearly twice that of the linear case and the overall appearance of the wave field differs considerably from that of the linear case.

The Stokes-type waves of different steepness values were also simulated by increasing the water depth to $h = 10$ m and adjusting the wave period so that the wavelengths would be the same as the other simulations. Increased water depth raised the relative depth to $h/L \simeq 1$, which is more appropriate for the deep water character of the Stokes waves. Since the Stokes waves are asymmetric compared to the linear waves but not as asymmetric as the cnoidal waves, the resulting wave patterns were expectedly between those of the linear and of the cnoidal waves. Therefore, observing no distinguished features, the figures of these simulations are excluded.

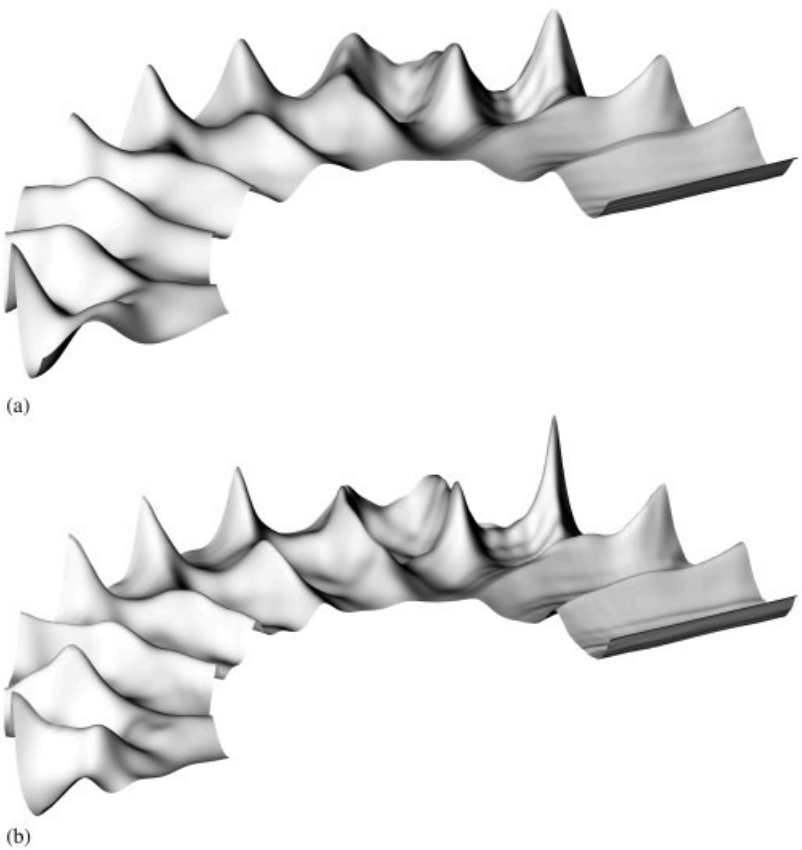

Figure 8. (a) Perspective view of the fully developed cnoidal wave field for $\varepsilon = 0.1$ at $t = 20T$ in a circular channel; and (b) Perspective view of the fully developed cnoidal wave field for $\varepsilon = 0.3$ at $t = 20T$ in a circular channel.

6. CONCLUDING REMARKS

Non-linear dispersive wave equations in boundary-fitted non-orthogonal curvilinear co-ordinates have been developed based on the one-component from of the wave model of Nadaoka *et al.* [13], which is valid for narrow-banded non-linear waves in arbitrary depths. Finite-difference approximations with a staggered grid system (Arakawa C-grid) is adopted for the numerical solution of the resulting boundary-fitted wave equations. Comparisons with the analytical solutions for gradually varying channels and circular channels provide convincing evidence, at least for linear wave fields, for the reliability and accuracy of the model equations and the numerical approach. The cnoidal waves in a circular channel are also simulated for two different wave steepness values to demonstrate the model's capability of simulating non-linear waves as well as revealing prominent differences compared to the linear case. As presented here, the model equations are capable of simulating narrow-banded non-linear wave motions in geometrically irregular regions. For practical uses, inclusion of the wave

breaking effect, albeit in a semi-empirical manner, is desirable especially in simulations involving nearshore regions.

ACKNOWLEDGEMENTS

This work was supported by the Research Funding Programme of Istanbul Technical University.

REFERENCES

1. Hoffmann KA, Chiang ST. *Computational Fluid Dynamics for Engineers* (3rd print), vols. 1 & 2. Engineering Education System: Wichita, Kansas, 1995.
2. Kantha LH, Clayson CA. *Numerical Models of Oceans and Oceanic Processes*. Academic Press: New York, 2000.
3. Johnson BH. VAHM-A vertically averaged hydrodynamic model using boundary-fitted coordinates. *MP HL-80-3* U.S. Army Engrs. Wtrwy. Experiment St., Vicksburg: Mississippi, 1980.
4. Spaulding ML. A vertically averaged circulation model using boundary-fitted coordinates. *Journal of Physical Oceanography* 1984; **14**:973–982.
5. Willemse JBTM, Stelling GS, Verbroom, GK. Solving the shallow water equations with an orthogonal co-ordinate transformation. *Delft Hydraulics Communication No.* 356, Delft Hydraulics Laboratory Delft, The Netherlands, 1985.
6. Muin M, Spaulding M. Two-dimensional boundary-fitted circulation model in spherical coordinates. *Journal of Hydraulic Engineering* 1996; **122**(9):512–521.
7. Sheng YP. Numerical modeling of coastal and estuarine processes using boundary-fitted grids. *Third International Symposium on River Sedimentation*, 1986; 1426–1442.
8. Bao XW, Yan J, Sun WX. A three-dimensional tidal wave model in boundary-fitted curvilinear grids. *Estuarine, Coastal and Shelf Science* 2000; **50**:775–788.
9. Hsu CT, Yeh KC, Yang JC. Depth-averaged two-dimensional curvilinear explicit finite analytic model for open channel flows. *International Journal for Numerical Methods in Fluids* 2000; **33**:175–202.
10. Li YS, Zhan JM. Boussinesq-type model with boundary-fitted coordinate system. *Journal of Waterway, Port Coastal and Ocean Engineering* 2001; **127**(3):152–160.
11. Romanenkov DA, Androsov AA, Voltzinger NE. Comparison of forms of the viscous shallow-water equations in the boundary-fitted coordinates. *Ocean Modelling* 2001; **3**:193–216.
12. Sankaranarayanan S, Spaulding ML. A study of the effects of grid non-orthogonality on the solution of shallow water equations in boundary-fitted coordinate systems. *Journal of Computational Physics* 2003; **184**:299–320.
13. Nadaoka K, Beji S, Nakagawa Y. A fully dispersive weakly nonlinear model for water waves. *Proceedings of the Royal Society of London A* 1997; **453**:303–318.
14. Beji S, Nadaoka K. A time-dependent nonlinear mild-slope equation for water waves. *Proceedings of the Royal Society of London A* 1997; **453**:319–32.
15. Engquist B, Majda A. Absorbing boundary conditions for the numerical simulation of waves. *Mathematics of Computation* 1977; **31**:629–51.
16. Bayliss A, Gunzburger M, Turkel E. Boundary conditions for the numerical solution of elliptic equations in exterior domains. *SIAM Journal on Applied Mathematics* 1982; **42**:430–51.
17. Grote MJ, Keller JB. On nonreflecting boundary conditions. *Journal of Computational Physics* 1995; **122**: 231–43.
18. Beji S, Nadaoka K. A formal derivation and numerical modelling of the improved Boussinesq equations for varying depth. *Ocean Engineering* 1996; **23**:691–704.
19. Arakawa A, Lamb VR. Computational design of the basic dynamical processes of the UCLA general circulation model. *Methods in Computational Physics* 1977; **17**:174–265.
20. Press WH, Flannery BP, Teukolsky SA, Vetterling WT. *Numerical Recipes*. Cambridge University Press: Cambridge, 1988; 797.
21. Lamb H. *Hydrodynamics*. Dover Publications: New York, 1932; 738.
22. Rostafinski W. Acoustic systems containing curved duct sections. *Journal of Acoustic Society of America* 1976; **60**:23–28.
23. Korteweg DJ, De Vries G. On the change of form of long waves advancing in a rectangular canal, and on a new type of long stationary waves. *Philosophical Magazine* 1895; **39**:422–43.

